Progress in Physics of Applied Materials 6 (2026), Serial Number 11, 163-178

Semnan University

Progress in Physics of Applied Materials

journal homepage: https://ppam.semnan.ac.ir/

An Examination from Fundamental Principles Regarding the Structural, Elastic, Electronic, Magnetic, and Optical Characteristics of F-Based Oxide full-Heusler Compounds

Saadiya Benatmane [a, b*]

[a]*Faculty of Sciences and Technology, Department of Science and Technology, BP227 Abdelhamid Ibn Badis University, 27000, Mostaganem, Algeria*
[b]*Laboratory of Modelling and Simulation of Materials Science, Djillali Liabès University of Sidi Bel-Abbès, 22000, Sidi Bel-Abbes, Algeria*

ARTICLE INFO

Article history:
Received: 22 November 2025
Revised: 13 December 2025
Accepted: 18 December 2025
Published online: 5 January 2026

Keywords:
d⁰ Half-metals;
First principles calculation;
WIEN2k;
Electronic properties;
Green energy.

ABSTRACT

This study presents a comprehensive investigation of the structural, electronic, magnetic, elastic, and optical properties of full-Heusler compounds O_2XF (X = Ca, Sr, Ba) using first-principles calculations based on density functional theory (DFT). The computations were carried out using the full-potential linearized augmented plane wave (FP-LAPW) method implemented in WIEN2k. The exchange–correlation potential was described using the generalized gradient approximation (GGA-PBE), while the Tran–Blaha modified Becke–Johnson (TB-mBJ) potential was applied to obtain accurate electronic structures. All compounds are found to crystallize in the Hg_2CuTi-type structure with a ferromagnetic ground state. Elastic constants calculated via the IRelast module confirm their mechanical stability and ductile nature. Band structure and density of states (DOS) analyses reveal half-metallic behavior: the majority-spin channel exhibits a semiconducting character, whereas the minority-spin channel remains metallic. The total magnetic moment of 3 μB per formula unit for all compounds agrees well with the Slater–Pauling rule Mtot=(24−Ztot) μB. Overall, the O_2XF (X = Ca, Sr, Ba) full-Heusler alloys are identified as mechanically robust half-metallic ferromagnets with 100% spin polarization, making them strong candidates for future spintronic and sustainable energy applications.

1. Introduction

Spintronics has emerged as a transformative field that goes beyond conventional charge-based electronics by exploiting the intrinsic spin of electrons in addition to their charge. This concept enables devices exhibiting nonvolatility, faster operation, lower power consumption, and reduced heat generation [1, 2].

In this context, half-metallic (HM) ferromagnets are of particular interest due to their complete spin polarization at the Fermi level, which significantly enhances spin injection efficiency in spintronic devices [3–6]. In HM materials, one spin channel displays metallic conductivity while the other exhibits a band gap at the Fermi level, resulting in 100% spin polarization [7]. Such unique behavior has been predicted for numerous material classes, including ferromagnetic oxides, diluted magnetic semiconductors, Zinc Blende compounds, and Heusler alloys [8–13]. For practical applications, HM ferromagnets must retain their half-metallic nature under mechanical strain and exhibit high Curie temperatures (Tc) to ensure stability at room temperature [14–16].

Among half-metallic materials, Heusler alloys stand out because of their high Curie temperatures, tunable electronic and magnetic properties, flexible crystal structures, and compatibility with semiconductor processing. (Materials

* Corresponding author.
E-mail address: saadia.benotmane@univ-mosta.dz

Cite this article as:
Benatmane, S., 2026. An Examination from Fundamental Principles Regarding the Structural, Elastic, Electronic, Magnetic and Optical Characteristics of F Based Oxide full-Heusler Compounds. *Progress in Physics of Applied Materials*, *6*(2), pp.163-178. DOI: 10.22075/ppam.2025.39751.1186

such as liquid metals are also employed in high-temperature environments as efficient heat conductors due to their superior thermal properties [17–19].) The concept of half-metallicity was first introduced by de Groot and collaborators in 1983 through their work on NiMnSb and PtMnSb alloys [20]. Since then, Heusler compounds have been widely studied for applications in superconducting devices, light-emitting systems, magnetic tunnel junctions (MTJs), and giant magnetoresistance (GMR) technologies [21–28].

Heusler materials are generally classified into ternary or quaternary intermetallic compounds [29]. Quaternary Heusler alloys, denoted as XX′YZ, consist of four interpenetrating face-centered cubic (fcc) sublattices located at sites A (0,0,0), B (0.25,0.25,0.25), C (0.5,0.5,0.5), and D (0.75,0.75,0.75). Recent research has increasingly focused on ferromagnetic compounds formed from abundant sp or d^0 elements, avoiding scarce transition metals. Several computational studies have predicted half-metallicity in such Heusler systems, including O_2BaX (X = Na, K, Rb, Cs) [30], XRbSr (X = Ge, C, Si) [31], NaKZ (Z = As, Sb, P, Ge) [32], LiXGe (X = Ba, Sr, Ca) [33], MNaCs (M = P, As) [34], N_2BaX (X = Rb, Cs, Ca, Sr) [35], and BaNYO (Y = Mg, Ca, Sr, K, Rb, Cs) [36,37].

The present investigation provides the first comprehensive first-principles analysis of the full-Heusler alloys O_2CaF, O_2SrF, and O_2BaF, composed exclusively of non–transition-metal elements. Using density functional theory (DFT) within the WIEN2k framework, we examine their structural, electronic, magnetic, mechanical, and optical properties. Calculations with and without spin polarization are performed to evaluate potential half-metallic characteristics. To the best of our knowledge, no previous theoretical or experimental studies have reported on these specific full-Heusler compounds.

2. Calculation Method

The crystallographic, electronic, and magnetic properties of the full-Heusler alloys O_2XF (with X = Ca, Sr, or Ba) were investigated using the WIEN2k software package [38], which employs the full-potential linearized augmented plane-wave (FP-LAPW) method [39]. Geometry optimizations and electronic structure calculations were performed within the generalized gradient approximation (GGA), using the Perdew–Burke–Ernzerhof (PBE) exchange–correlation functional [40].

The energy threshold separating core and valence states was set to –6.0 Ry. Core states were treated fully relativistically, whereas valence electrons were described using a semi-relativistic approximation. Brillouin-zone integrations were carried out using a 4000 k-point mesh to ensure reliable convergence. The basis-set size was controlled by an RMTKmax value of 9.0, where RMT denotes the smallest muffin-tin radius and Kmax is the maximum reciprocal-lattice vector in the plane-wave expansion. Total energies were converged to within 10^{-4} Ry.

3. Results and Discussion

3.1. Structural Properties

Full-Heusler compounds typically follow the chemical formula X_2YZ, where X and Y are usually transition metals and Z is a p-block element. These materials crystallize in one of two cubic structures: the $L2_1$ type, analogous to Cu_2MnAl (space group $Fm\bar{3}m$, No. 225), or the XA type, similar to Hg_2CuTi (space group $F\bar{4}3m$, No. 216). Figure 1 demonstrates the crystal structure of O_2XF (X=Ca, Sr, and Ba) Heusler alloys: Cu_2AlMn-type and Hg_2CuTi-type.

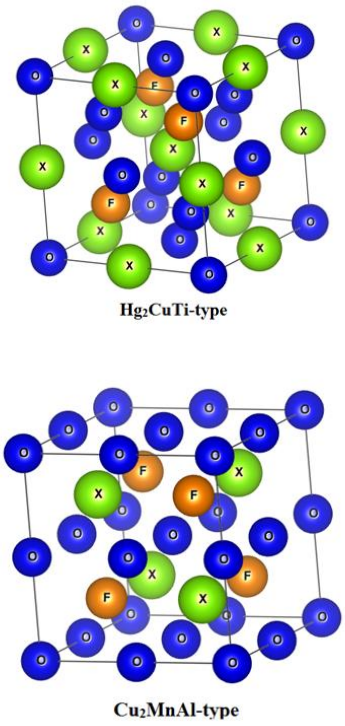

Fig. 1. Crystal structure of O_2XF (X=Ca, Sr, and Ba) Heusler alloys: Cu_2AlMn-type and Hg_2CuTi-type.

The $L2_1$ structure consists of four interpenetrating face-centered cubic (fcc) sublattices. In this arrangement, the X atoms occupy the Wyckoff position 8c (0.25, 0.25, 0.25), Y is located at 4b (0.5, 0.5, 0.5), and Z at 4a (0, 0, 0). Consequently, the X atoms fill the B (0.25, 0.25, 0.25) and D (0.75, 0.75, 0.75) sites, while Y and Z are situated at the C (0.5, 0.5, 0.5) and A (0, 0, 0) sites, respectively [Table 1].

In contrast, the XA structure (Hg_2CuTi-type) features two inequivalent X atoms, labeled X_1 and X_2, positioned at the Wyckoff sites 4a (0, 0, 0) and 4b (0.25, 0.25, 0.25). The Y and Z atoms occupy the 4c (0.5, 0.5, 0.5) and 4d (0.75, 0.75, 0.75) positions, respectively. This distinct atomic ordering strongly influences the electronic and magnetic properties, highlighting the importance of structural stability for practical applications.

To assess the lattice stability of O_2CaF, O_2SrF, and O_2BaF, total energies were calculated as a function of unit-cell volume under both non-magnetic and ferromagnetic configurations [Fig. 2]. The results indicate that the ferromagnetic state is energetically favored. In the optimized XA-type structures, oxygen atoms occupy the C sites, the X atoms (Ca, Sr, Ba) reside at the B sites, and fluorine atoms are located at the A sites.

Equilibrium lattice parameters (a_0), bulk moduli (B), and their pressure derivatives (B′) were obtained by fitting the energy–volume data to the Birch–Murnaghan equation of state [42], with the corresponding values summarized in Table 2. For the XA-type phase, the calculated lattice constants are 5.71 Å for O_2CaF, 5.99 Å for O_2SrF, and 6.31 Å for O_2BaF. This increasing trend reflects the larger ionic radii of the X-site atoms.

Cohesive energy (E_c) and formation enthalpy (E_f) were also evaluated to determine the chemical and thermal stability of these compounds. Both quantities exhibit negative values, confirming that the O_2XF alloys are energetically favorable and potentially synthesizable.

With structural stability established, we proceeded to examine the mechanical, electronic, optical, and magnetic properties of the O_2XF (X = Ca, Sr, Ba) alloys in their XA configuration, providing a comprehensive understanding of their potential for advanced technological applications.

$$E_c^{\mathrm{O2XF}} = E_{tot}^{\mathrm{O2XF}} - (2E_O + E_X + E_F) \quad (1)$$

In this equation, E_{tot}^{O2XF} denotes the balanced total energy for the O_2XF alloys, whereas E_O, E_X (X = Ca, Sr, Ba), and E_F represent the overall energies of the corresponding free atoms. Each isolated atom's energy was computed employing a face-centered cubic (FCC) crystal structure featuring a lattice constant of 20 atomic units.

The formation energy determines the thermodynamical stability and used to previse whether the material can be synthesised experimentally. The formation energy is given by :

$$E_f^{O2XF} = E_{tot}^{O2XF} - (2E_O + E_X + E_F) \quad (2)$$

where E_{tot}^{O2XF} represents the total ground-state energy per formula unit of O_2XF, and E_O, E_X, and E_F denote the ground-state energies of the constituent O, X, and F atoms, respectively. The calculated formation energies of the O_2XF compounds are reported in Table 2. The negative values of E_f indicate thermodynamic stability, suggesting that these materials are experimentally synthesizable. The calculated Debye temperatures (θ_D) for the studied compounds are listed in Table 3.

The computed cohesive energy (E_c) and formation enthalpy (E_f) for all compounds in the cubic phase are also summarized in Table 2. The presence of negative values for both E_c and E_f confirms the strong chemical bonding and thermodynamic stability of the O_2XF series, indicating that these compounds are highly promising candidates for experimental realization.

3.2. Elastic properties

Understanding the elastic properties of materials is essential for gaining insights into their bonding characteristics, anisotropic behavior, and overall structural integrity. In particular, the elastic constants provide valuable information about internal atomic interactions and the mechanical performance of crystalline solids. By calculating these constants (C_{ij}), one can assess both the mechanical stability and the response of a material to external stresses.

In this study, the primary elastic constants C_{11}, C_{12}, and C_{44} were calculated for the cubic fluoride compounds O_2CaF, O_2SrF, and O_2BaF using the IRelast module of the WIEN2k software package [43]. These moduli characterize the lattice response to different deformation modes: C_{11} measures resistance to uniaxial stress, C_{12} reflects the response to uniform volumetric strain, and C_{44} quantifies resistance to pure shear deformation. The numerical values, presented in Table 4, confirm the structural robustness of the investigated phases.

Understanding the elastic properties of materials is essential for gaining insight into their bonding characteristics, anisotropic behavior, and overall structural integrity. In particular, the elastic constants provide valuable information about internal atomic interactions and the mechanical performance of crystalline solids. By calculating these constants (C_{ij}), both the mechanical stability and the response of a material to external stresses can be assessed.

In this study, the primary elastic constants C_{11}, C_{12}, and C_{44} were calculated for the cubic fluoride compounds O_2CaF, O_2SrF, and O_2BaF using the IRelast module of the WIEN2k software package [43]. These moduli characterize the lattice response to different deformation modes: C_{11} measures the resistance to uniaxial stress, C_{12} reflects the response to uniform volumetric strain, and C_{44} quantifies resistance to pure shear deformation. The numerical values, presented in Table 4, confirm the structural robustness of the investigated phases

- C_{11} positive
- C_{44} positive
- $C_{11} - C_{12} > 0$
- $C_{11} + 2C_{12} > 0$
- C_{12} < bulk modulus B < C_1

A solid's mechanical reliability is governed by its elastic behavior, a prerequisite for virtually every engineering use. Consequently, the measured elastic constants act as quantitative yardsticks of the material's load-bearing capacity, estimating mechanical parameters such as the bulk modulus $B = \frac{C_{11}+2C_{12}}{3}$, Voigt ($G_V$) and Reuss ($G_R$) polycrystalline elastic modulus are given as follows $G_V = \frac{C_{11}-C_{12}\mp 3C_{44}}{5}$, $G_R = \frac{5(C_{11}-C_{12})C_{44}}{4C_{44}+3(C_{11}-C_{12})}$, while the shear modulus $G_H = \frac{G_R+G_V}{2}$ serves as a gauge of the material's resistance to shape-changing (shear) forces.

In addition to the elastic constants, several derived properties were calculated to provide a more comprehensive understanding of the materials' mechanical behavior. These properties include the anisotropy parameter (A), Cauchy's pressure (C″), Kleinman factor (ζ),

Young's modulus (E), and Poisson's ratio (ν). They were determined using the following equations:

Anisotropy parameter : $A = \frac{2C_{44}}{C_{11}-C_{12}}$

Cauchy's pressure : $C'' = C_{12} - C_{44}$

Kleinman factor : $\zeta = \frac{C_{11}+8C_{12}}{7C_{11}+2C_{12}}$

Young's modulus : $E = \frac{9BG}{3G+B}$

Poisson's ratio : $\nu = \frac{3B-2G}{2(3B+G)}$.

Young's modulus (E) quantifies a material's resistance to elastic deformation. Among the studied compounds, O_2BaF exhibits the highest Young's modulus, indicating the greatest stiffness, followed by O_2CaF and O_2SrF. The bulk modulus (B) further reflects the material's resistance to volumetric compression.

The ductility or brittleness of the materials was assessed using Pugh's ratio (B/G), where values above 1.75 indicate ductile behavior [45]. All three compounds were found to be ductile, making them suitable for applications involving mechanical stress. This conclusion is reinforced by Poisson's ratio (ν > 0.25), suggesting predominantly ionic bonding, and by positive Cauchy pressures [46].

The elastic anisotropy factor (A) indicates the degree of directional dependence in elastic behavior. A value of A = 1 corresponds to isotropic elasticity, whereas deviations from 1 reflect anisotropic behavior. As shown in Table 4, the compounds exhibit varying degrees of anisotropy: O_2BaF is the closest to isotropic behavior, while O_2SrF shows the highest anisotropy. This variation implies differences in how mechanical properties change along different crystallographic directions.

The Debye temperature (θ_D) is a critical parameter for understanding the thermodynamic and vibrational properties of solids, including specific heat, melting temperature, elastic stiffness, and thermal conductivity [61]. A higher θ_D typically indicates stronger bonding, higher thermal conductivity, and a higher melting point.

At low temperatures, lattice vibrations are dominated by acoustic phonon modes, which are closely linked to the Debye temperature. One reliable approach to estimate θ_D relies on elastic constants and derived parameters related to the material's average sound velocity (v_m). This velocity depends on both longitudinal and shear wave velocities, which can be calculated from the elastic constants C_{11}, C_{12}, and C_{44}.

This method, which often yields results comparable to specific-heat measurements [47, 48], allows precise determination of the Debye temperature using only elastic data. Consequently, by analyzing the elastic properties of O_2BaF, O_2CaF, and O_2SrF, θ_D can be calculated to provide insights into their thermal behavior and conductivity. The following classical relation can be employed for this estimation [49, 50]:

$$\theta_D = \frac{h}{k_B}\left(\frac{3n}{4\pi}\frac{N_A\rho}{M}\right)^{\frac{1}{3}}\upsilon_m \quad (3)$$

Here, h represents Planck's constant, k_B denotes Boltzmann's constant, N_A is Avogadro's number, ρ signifies the density, M stands for the molar mass, and n indicates the number of atoms within the unit cell. From specific heat measurements, θ_D can be determined via the subsequent relation [51]:

$$\theta_D = \left(\frac{200}{V^{\frac{1}{3}}}\right)\left(\sqrt{\frac{T_m}{M}}\right) \quad (4)$$

In this equation, V represents the molar volume (in cm^3/mol), M is the molar mass (in g/mol), and T_m denotes the melting point (in Kelvin). For polycrystalline materials, the average sound velocity v_m can be computed using the following formula [49, 52]:

$$\upsilon_m = \left[(2\upsilon_t^{-3} + \upsilon_l^{-3})/3\right]^{-1/3} \quad (5)$$

Here, v_t and v_l correspond to the transverse and longitudinal elastic wave velocities, respectively. These velocities can be derived from the shear modulus G, the bulk modulus B, and the density ρ by applying Navier's equation, as detailed in references [53–55] and given below:

$$\upsilon_m = \left[(2\upsilon_t^{-3} + \upsilon_l^{-3})/3\right]^{-1/3} \quad (6)$$

$$\upsilon_l = \left[\left(3B + 4G\right)/(3\rho)\right]^{1/2} \quad (7)$$

Table 3 presents the computed values for transverse sound velocity (v_t), longitudinal sound velocity (v_l), mean sound velocity (v_m), and Debye temperature (θ_D) for the O_2CaF, O_2SrF, and O_2BaF compounds in the Hg_2CuTi phase. These calculations are essential for predicting the thermal behavior and mechanical stability of these materials.

The Debye temperature (θ_D) is notably higher in O_2BaF compared to O_2CaF and O_2SrF, suggesting a stiffer crystal lattice and a potentially higher melting point. This indicates that O_2BaF possesses a more rigid structure, requiring greater energy to excite phonons, and is therefore well suited for applications demanding thermal resistance, such as thermoelectric power generation.

Moreover, a Debye temperature above 300 K typically signifies high thermal conductivity within a material. Although the Debye temperatures for the studied compounds are slightly below 300 K (281.74 K for O_2BaF, 221.99 K for O_2CaF, and 165.72 K for O_2SrF), they still exhibit relatively high thermal conductivity. This makes these compounds promising candidates for thermal management applications, where efficient heat dissipation is crucial.

Given the lack of prior theoretical or experimental documentation of these materials, the findings presented here offer a valuable reference for future experimental and theoretical studies. The high θ_D values, particularly in O_2BaF, highlight the potential of these compounds for thermoelectric and high-temperature applications.

Table 1. The preference in ordering between the standard L21 structure (specifically Cu_2MnAl) and the inverted XA arrangement (as exemplified by Hg_2CuTi for O_2XF (X=Ca, Sr and Ba) compounds, is determined by the occupants assigned to the four designated Wyckoff positions: A at (0, 0, 0), B at (0.25, 0.25, 0.25), C at (0.5, 0.5, 0.5), and D at (0.75, 0.75, 0.75).

Type/Atom	O	O	(X=Ca, Sr and Ba)	F
L21	4b (0.25, 0.25, 0.25)	4d (0.75, 0.75, 0.75)	4c (0.5, 0.5, 0.5)	4a (0, 0, 0)
XA	4a (0, 0, 0)	4c (0.5, 0.5, 0.5)	4b (0.25, 0.25, 0.25)	4d (0.75, 0.75, 0.75)

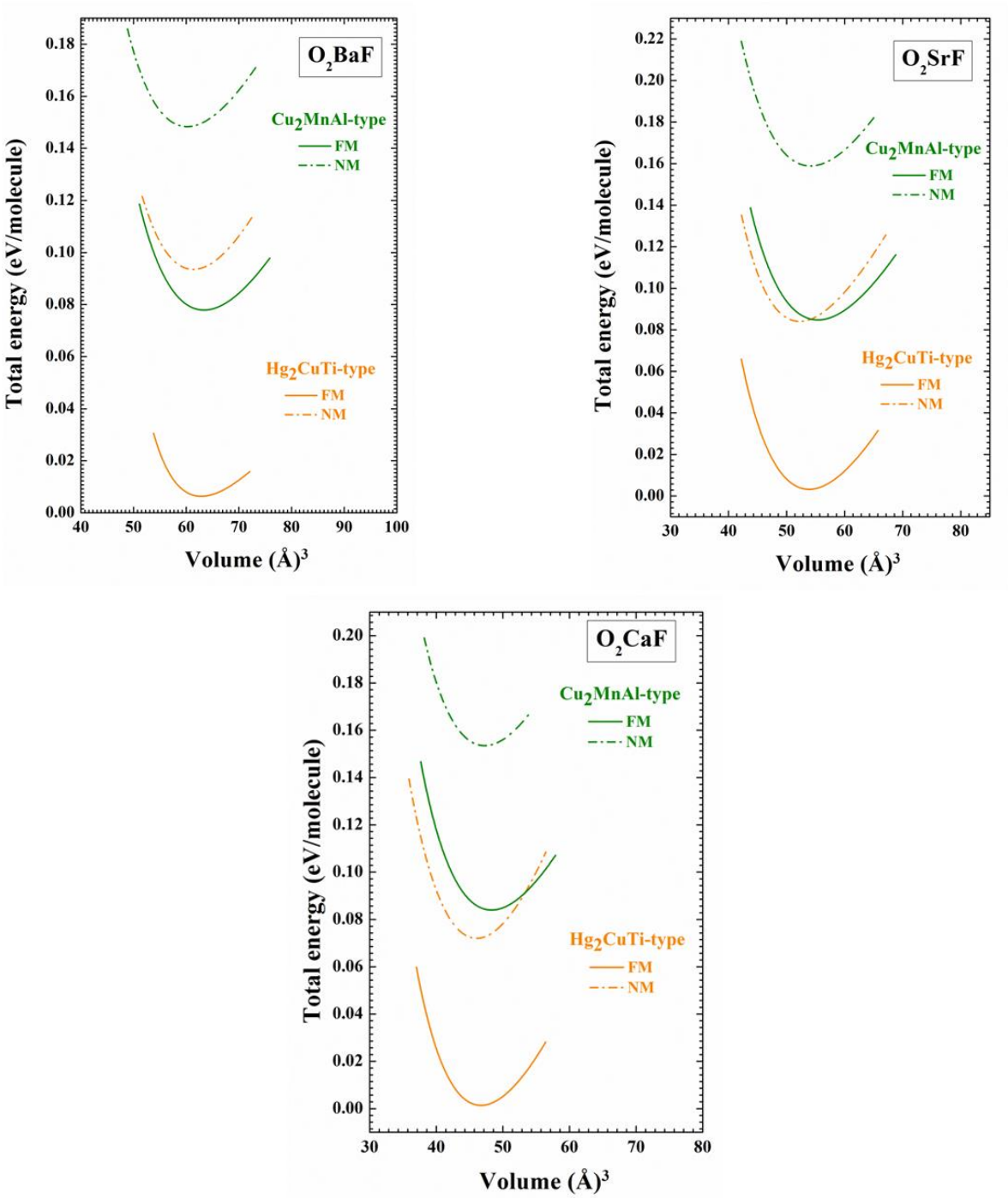

Fig. 2. Total energies as functions of volume per formula unit are compared for the ferromagnetic (FM) and non-magnetic (NM) states for the O_2XF (X=Ca, Sr, and Ba) Heusler alloys using the GGA-PBE approximation, in the Cu_2MnAl and Hg_2CuTi-type structures.

Table 2. The equilibrium lattice constant (a), bulk modulus (B), its pressure derivative (B'), cohesive energy (E_c) in electron volts (eV), formation energy (E_f) also in eV, and the energy separation $\Delta E=E_{NM}-E_{FM}$ (eV) have been determined for compounds denoted as O_2XF compounds where X represents Ca, Sr and Ba. These calculations consider both the ferromagnetic (FM) and non-magnetic (NM) spin configurations within the framework of the generalized gradient approximation with the Perdew-Burke-Ernzerhof prescription (GGA-PBE) for structures analogous to Cu_2MnAl and Hg_2CuTi-type.

Compound	structure	Method		*a* (Å)	*B* (GPa)	*B'*	E_c (Ry)	E_f (Ry)	ΔE (Ev)
O_2BaF	Hg_2CuTi	GGA-PBE	FM	6.31	54	5.14	-1.48	-0.72	1.18
			NM	6.25	59	4.52	-1.39	-0.66	
	Cu_2MnAl		FM	6.33	50	4.49	-1.41	-0.68	
		GGA-PBE	NM	6.22	52	4.55	-1.34	-0.61	
O_2CaF	Hg_2CuTi		FM	5.71	80	4.55	-1.47	-0.74	0.95
			NM	5.68	92	3.40	-1.40	-0.67	
	Cu_2MnAl	GGA-PBE	FM	5.78	74	4.49	-1.39	-0.66	
			NM	5.73	78	4.42	-1.32	-0.59	
O_2SrF	Hg_2CuTi		FM	5.99	70	4.46	-1.46	-0.75	1.10
		GGA-PBE	NM	5.93	73	5.14	-1.39	-0.67	
	Cu_2MnAl		FM	6.05	62	4.51	-1.39	-0.67	
			NM	6.00	64	4.46	-1.31	-0.60	

Table 3. The longitudinal (v_l), transverse (v_t), and mean (v_m) sound velocities, expressed in meters per second (m/s), along with the Debye temperature (Θ_D) in Kelvin (K), for the O_2XF compounds where X represents Ca, Sr and Ba.

Compound	v_l	v_t	v_{avg}	Θ_D
O_2BaF	4103.05	2116.84	2370.13	281.74
O_2CaF	5268.99	1783.61	1692.04	221.99
O_2SrF	4277.8	1160.61	1324.18	165.72

Table 4. Elastic parameters C_{ij} (in GPa), along with the bulk modulus B (GPa), shear modulus G (GPa), Young's modulus E (GPa), Poisson's ratio ν, degree of anisotropy A, the ratio B/G (Pugh's ratio), and Cauchy pressure C'' (all in GPa), determined for the O_2XF compounds where X represents Ca, Sr and Ba.

Compound	C_{11}	C_{12}	C_{44}	B_V	B_R	B_H	G_V	G_R	G_H	E	A	ν	B/G	C''
O_2BaF	80.35	40.88	24.19	54.04	54.04	54.04	22.41	22.18	22.29	58.80	1.22	0.31	2.42	16.69
O_2CaF	112.82	64.08	2.06	80.33	80.33	80.33	10.98	3.25	7.12	20.75	0.08	0.45	11.28	62.02
O_2SrF	99.25	56.19	1.32	70.54	70.54	70.54	9.40	2.11	5.75	16.81	0.061	0.46	12.26	54.87

3.3. Electronic properties

Calculations for the electronic band structures of the O_2XF series (with X = Ca, Sr, Ba) were performed at their optimized lattice parameters, utilizing both the GGA-PBE and mBJ-GGA approximations, as visualized in Figures 3 through 5. These plots illustrate the allowed electronic energy states along designated high-symmetry paths traversing the initial Brillouin zone, specifically emphasizing the Hg_2CuTi-type. Structural motif across the W, L, Λ, Γ, Δ, X, Z, W, and K vectors. Investigation covered both the majority (spin-up) and minority (spin-down) spin projections.

Calculations for the electronic band structures of the O_2XF series were performed at their optimized lattice parameters, utilizing both the GGA-PBE and mBJ-GGA approximations, as visualized in Figures 3 through 5. These plots illustrate the allowed electronic energy states along high-symmetry paths traversing the first Brillouin zone, specifically emphasizing the Hg_2CuTi-type structural motif across the W, L, Λ, Γ, Δ, X, Z, W, and K points. Both majority (spin-up) and minority (spin-down) spin channels were investigated.

The calculated band structures reveal that the Fermi level intersects only the minority-spin bands, while a well-defined band gap exists in the majority-spin channel, confirming the half-metallic nature of the O_2XF compounds. In this context, two key quantities must be distinguished to correctly characterize the electronic behavior: the spin-resolved fundamental band gap ($E_{(g)}$) and the half-metallic band gap ($E_(HM)$). The conventional band gap, $E_{(g)}$, corresponds to the energy difference between the valence-band maximum (VBM) and the conduction-band minimum (CBM) within the same spin channel. For all compositions, this gap appears exclusively in the spin-up channel, indicating that the majority-spin electrons exhibit semiconducting behavior. In contrast, the minority-spin channel remains metallic due to bands crossing the Fermi level.

The half-metallic gap ($E_(HM)$) is defined as the smallest energy separation between the CBM (of the gapped spin channel) and the Fermi level, or between the Fermi level and the VBM, depending on which is smaller. This quantity determines the energetic stability of the half-metallic state: larger $E_(HM)$ values indicate greater robustness against thermal excitations, spin fluctuations, and structural perturbations that could otherwise destroy full spin polarization. The values listed in Table 5 show that O_2SrF exhibits the largest $E_{(g)}$, while O_2CaF presents the highest $E_(HM)$, indicating particularly robust half-metallic behavior. Moreover, the TB-mBJ functional systematically enhances both $E_{(g)}$ and $E_(HM)$ compared to GGA-PBE,

reflecting its improved description of the exchange potential and its ability to open more realistic band gaps, particularly near the Γ point.

Overall, the presence of a finite $E_{(g)}$ exclusively in the majority-spin channel, combined with a nonzero $E_(HM)$ and metallic minority-spin states, provides unambiguous evidence that the O_2XF compounds are true half-metallic ferromagnets with strong spin polarization at the Fermi energy.

The results reveal that in the minority-spin channel, the energy bands cross the Fermi level, whereas in the majority-spin channel, this level resides clearly within a forbidden energy region (band gap). This behavior demonstrates full spin polarization at the Fermi energy, thereby confirming the ferromagnetic half-metallic (HM) nature of these materials. Owing to the strong similarity among the calculated band structures, the following discussion primarily focuses on the O_2BaF compound, assuming the Hg_2CuTi-type crystal structure.

For O_2BaF, the minority-spin channel comprises six bands extending from −1.08 eV to 1.18 eV. In contrast, the majority-spin channel contains six bands located between −3.74 eV and −0.89 eV, which are mainly derived from the oxygen p orbitals. Additionally, three distinct bands appearing in the energy range −9.5 eV to −8.7 eV, present in both spin channels, originate from the fluorine p states. Finally, three deeper bands, localized between −17 eV and −16 eV, can be attributed to the barium p orbitals.

The key parameters characterizing half-metallic materials are the fundamental band gap ($E_{(g)}$), associated with either the majority- or minority-spin channel, and the half-metallic gap ($E_(HM)$). The conventional band gap, $E_{(g)}$, is defined as the energy difference between the valence-band maximum (VBM) and the conduction-band minimum (CBM) within a given spin channel. In contrast, $E_(HM)$ represents the minimum energy separation between the CBM or VBM and the Fermi level, depending on which is closer. Our calculations indicate that the band gap opens exclusively in the spin-up (majority) channel, thereby confirming the presence of a majority-spin band gap.

Table 5 summarizes the calculated $E_{(g)}$ and $E_(HM)$ values for the O_2XF series. O_2SrF exhibits the largest $E_{(g)}$, indicating greater resistance to external perturbations, such as temperature or pressure variations. In contrast, O_2CaF displays the highest $E_(HM)$, implying an exceptionally robust half-metallic character. The significant $E_(HM)$ values obtained using both GGA-PBE and mBJ-GGA approaches highlight the intrinsic stability of the half-metallic state against external disturbances. Furthermore, the TB-mBJ functional efficiently opens the band gap at the Γ point, resulting in a more accurate representation of the electronic structure.

To further elucidate the electronic characteristics of the O_2XF compounds, we analyzed the total and partial density of states (DOS) for the Hg_2CuTi-type configuration. Figures 6–8 display the DOS distributions for O_2BaF, O_2CaF, and O_2SrF, respectively, clearly revealing the orbital-resolved contributions to the electronic structure.
The presence of minority-spin states at the Fermi level, together with a distinct band gap in the majority-spin channel, provides additional confirmation of the half-metallic nature of these alloys. In the majority-spin channel, electronic states in the energy window −3.64 eV to −0.98 eV are dominated by oxygen and fluorine p orbitals. Similarly, in the minority-spin channel, states ranging from −2.47 eV to 0.98 eV originate primarily from the same atomic orbitals.

The formation of the majority-spin band gap can be attributed to two fundamental mechanisms. First, the weak hybridization and limited orbital overlap among the O, X (Ca, Sr, Ba), and F atoms near the Fermi level facilitate the opening of the gap. Second, the exchange-splitting effect separates the spin-up and spin-down states, shifting the majority-spin states to lower energies below the Fermi level while pushing the minority-spin states upward. As a result, the Fermi level intersects only the minority-spin bands, producing a stable and well-defined half-metallic state.

In summary, the DOS analysis fully supports the conclusions drawn from the band-structure calculations, unequivocally demonstrating a spin-polarized electronic configuration. These findings confirm that the O_2XF compounds are stable

Co_2-based full Heuslers (e.g., Co_2MnSi, Co_2FeSi) are prototypical half-metals with large Curie temperatures and magnetic moments that often closely follow Slater–Pauling, they remain metallic in one spin channel with a minority (or majority, by convention) gap that can be affected by disorder and pressure. These materials illustrate how robust exchange splitting and favorable hybridization lead to large T_C and stable half-metallicity a useful contrast for O_2XF, which gains its gap through weaker p–d (O/X/F) hybridization and exchange splitting rather than strong d–d bonding.

3.4. Magnetic Properties

For the O_2XF compounds, where (X = Ca, Sr, Ba), the calculated total magnetic moment at the equilibrium lattice spacing consistently registers as 3.00 μB per unit cell, regardless of whether the GGA-PBE or mBJ-GGA methods are employed. This value strongly indicates a ferromagnetic ground state, a conclusion supported by the fact that the moment is an exact integer. The specifics of these total magnetic moments, broken down into contributions from individual atoms alongside any moments found in the interstices of the unit cell, are detailed in Table 5.

The bulk of the magnetic moment originates with the oxygen and fluorine atoms, mainly due to the significant exchange splitting observed between the spin-up and spin-down electronic states of oxygen. Within certain chemical structures, the localized magnetic moments associated with sp atoms orient oppositely to those of O and F, leading to a ferrimagnetic contribution.

For alloys possessing the full-Heusler structure, the overall spin magnetic moment adheres to the extended Slater–Pauling relationship. More precisely, the cumulative magnetic moment per equivalent unit (Mtot) is connected to the overall count of valence electrons (Ztot) according to the formula:

$$M_{tot} = Z_{tot} - 24 \quad (8)$$

The calculated total magnetic moment satisfies the rule of the Slater-Pauling behavior in the full-Heusler alloys. In this rule, Mtot is related to total valence electrons (Z_{tot}) of

alloys. In order to obtain Slater-Pauling equations for HM O_2XF (X = Ca, Sr, Ba) compounds, the band structures of these alloys should be considered. The majority spin bands are occupied with 12 electrons (8 spin p and 4 spin s of the two atoms of O) Thus, the number of occupied minority states (N↓) is calculated as:

$$N\downarrow = Z_{tot} - N\uparrow = Z_{tot} - 12 \quad (9)$$

where N↑ is the number of occupied majority (spin-up) states. Therefore, Mtot is calculated as:

$$M_{tot} = (N\downarrow - N\uparrow)\ \mu B = (2N\uparrow - Z_{tot})\ \mu B = (24 - Z_{tot})\ \mu B \quad (10)$$

O_2XF (X = Ca, Sr, Ba) compounds have 21 valence electrons (Z_{tot}=21, 12 from the two O atoms, 2 from (Ca, Sr, Ba) and 7 from F), according to equation (10) M_{tot} obtained equal to 3 μB for the O_2XF which are in a good agreement with the results of Table 5, as expected, all HM ferromagnets investigated exhibit an integer magnetic moment.

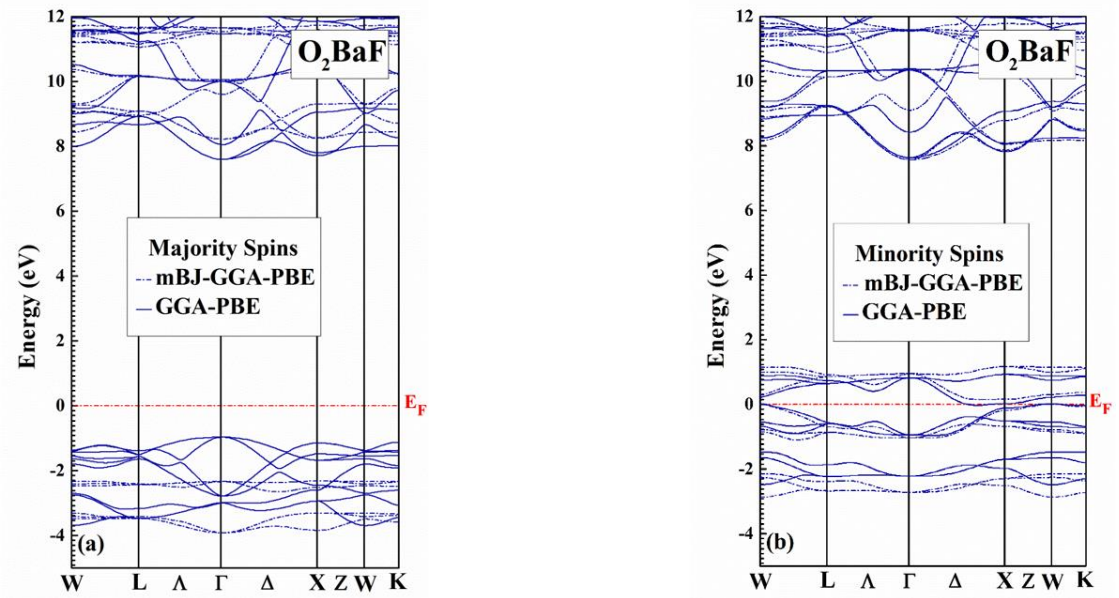

Fig. 3. Comparison of GGA-PBE and mBJ-GGA-PBE spin-polarized band structures (*a*) spin up, and (*b*) spin down of O_2BaF, calculated at the equilibrium lattice constant. The horizontal dashed line indicates the Fermi level.

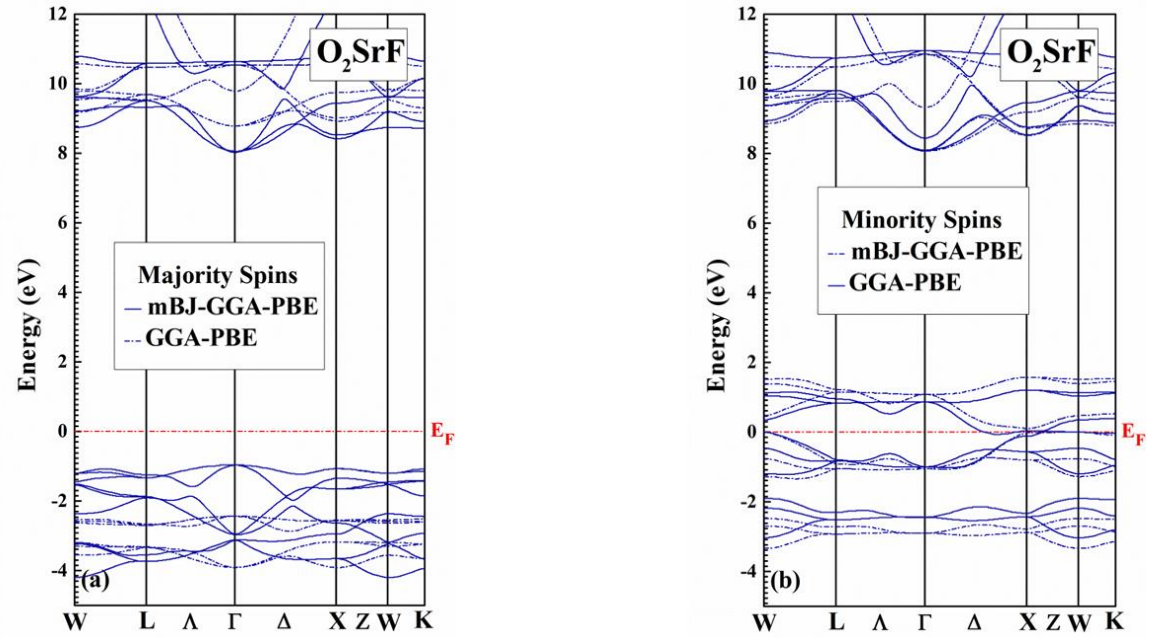

Fig. 4. Comparison of GGA-PBE and mBJ-GGA-PBE spin-polarized band structures (*a*) spin up, and (*b*) spin down of O_2SrF, calculated at the equilibrium lattice constant. The horizontal dashed line indicates the Fermi level.

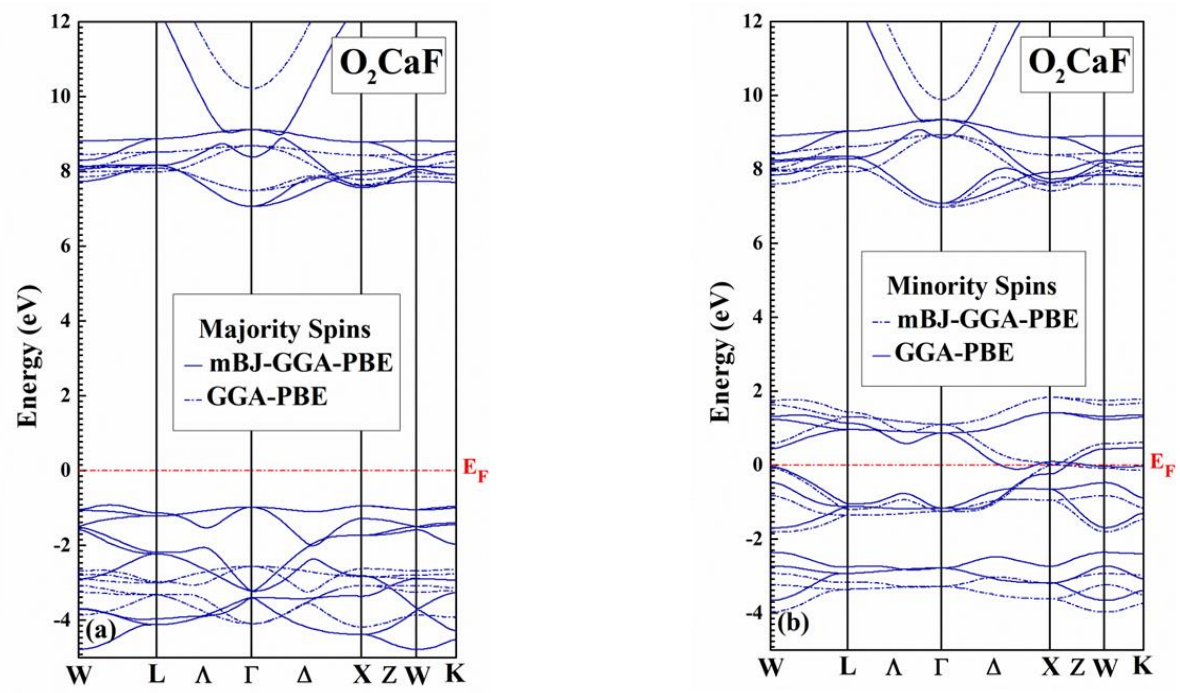

Fig. 5. Comparison of GGA-PBE and mBJ-GGA-PBE spin-polarized band structures (*a*) spin up, and (*b*) spin down of O_2CaF, calculated at the equilibrium lattice constant. The horizontal dashed line indicates the Fermi level.

Table 5. The magnetic moments, both total, partial, and interstitial, calculated per formula unit for the O_2XF compounds where X represents Ca, Sr and Ba, along with their half-metallic gaps (HM) in eV and energy gaps (E_g) in eV, as determined by the GGA-PBE and mBJ-GGA-PBE methods.

	Methods	μ_{inters} **(μB)**	μ_O **(μB)**	μ_F **(μB)**	μ_X ***(X=Ba, Ca, Sr)*** **(μB)**	μ_{tot} **(μB)**	**HM gap (eV)**	E_g **(eV)**	**Band gap**
O_2BaF	GGA-PBE	0.41	1.38	0.14	0.01	3.00	0.96	8.57	direct (Γ -Γ)
	mBJ-GGA-PBE	-0.04	1.69	0.11	0.01	3.00	2.33	10.56	
O_2CaF	GGA-PBE	0.37	1.44	0.18	0.00	3.00	1.00	8.05	direct (Γ- Γ)
	mBJ-GGA-PBE	-0.07	1.77	0.15	-0.01	3.00	2.60	10.08	
O_2SrF	GGA-PBE	0.39	1.41	0.16	0.00	3.00	0.93	8.96	direct (Γ - Γ)
	mBJ-GGA-PBE	-0.07	1.74	0.13	-0.00	3.00	2.43	11.24	

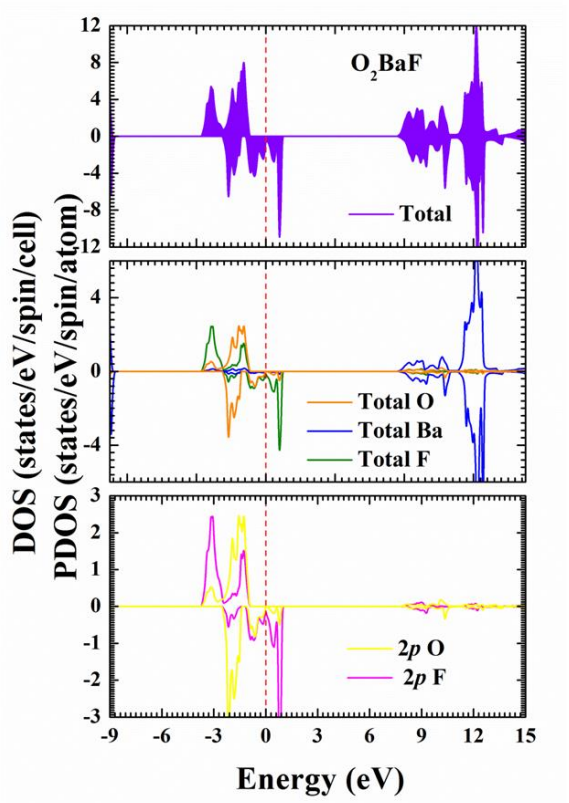

Fig. 6. Spin-dependant total and partial densities of states for O_2BaF. The vertical dashed line indicates the Fermi level. Positive and negative values of DOS hold for spin-up and spin-down states, respectively.

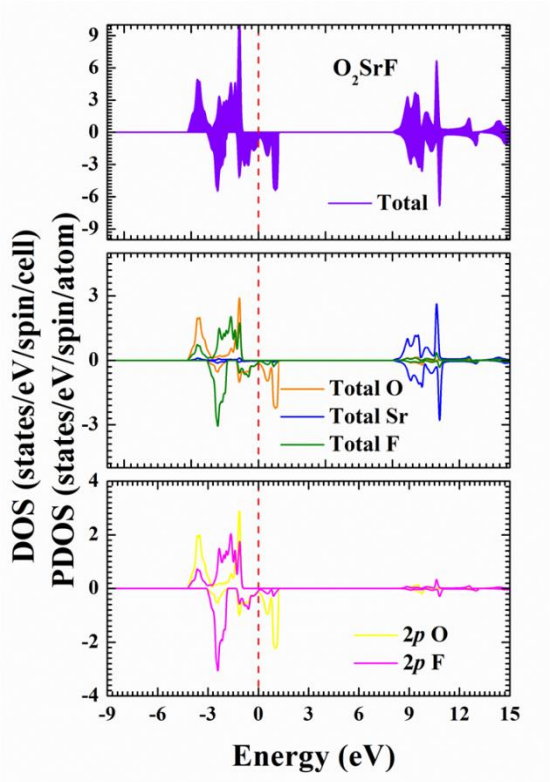

Fig. 7. Spin-dependant total and partial densities of states for O_2SrF. The vertical dashed line indicates the Fermi level. Positive and negative values of DOS hold for spin-up and spin-down states, respectively.

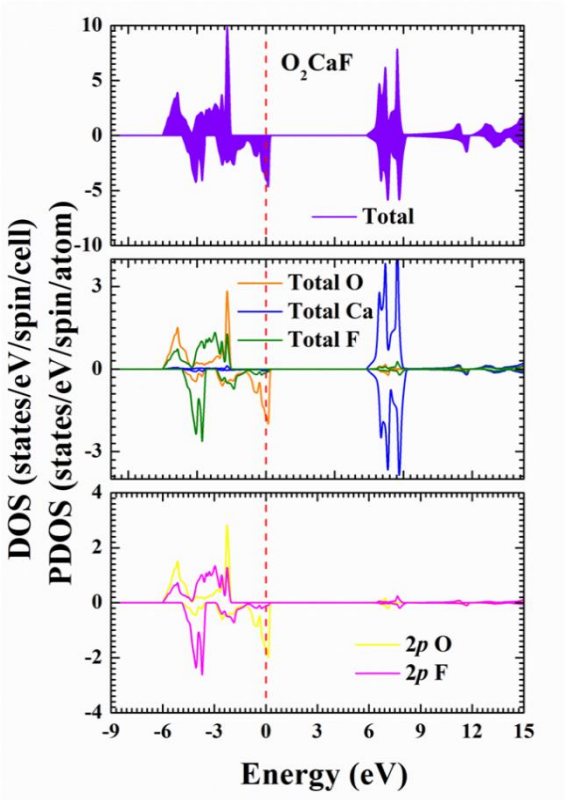

Fig. 8. Spin-dependant total and partial densities of states for O_2CaF. The vertical dashed line indicates the Fermi level. Positive and negative values of DOS hold for spin-up and spin-down states, respectively.

3.5. Optical Properties

The equilibrium lattice parameters, which are derived theoretically, serve as the basis for investigating the entirety of optical properties. The complete set of optical features can be thoroughly analyzed by means of the dielectric function, ε (ω).

3.5.1. Dielectric function (The real and imaginary part)

The real component of the dielectric constant reveals how much a material polarizes, conversely, its imaginary part signifies the energy dissipated within the dielectric system [59]. Determining the loss tangent involves calculating the quotient of the imaginary part by the real part, which serves as an indicator of the energy absorbed by the material. The entire dielectric function, which varies with frequency, denoted as ε(ω), is structured as follows:

$\varepsilon(\omega) = \varepsilon_1(\omega) + i\,\varepsilon_2(\omega)$. Here, $\varepsilon_1(\omega)$ denotes the real term, and $\varepsilon_2(\omega)$ represents the imaginary term.

The computed real $\varepsilon_1(\omega)$ and imaginary $\varepsilon_2(\omega)$ parts of the dielectric function for O_2XF structures, derived via the GGA-PBE functional, are depicted across figures 9 through 11, covering photon energies extending to 30eV. Specifically, the $\varepsilon_1(\omega)$ term governs the extent of wave damping and energy loss, while the $\varepsilon_1(\omega)$ corresponds to the materials' capacity for polarization and the storage of energy.

When the photon energy approaches zero, the static dielectric constants, denoted as $\varepsilon_1(0)$, are calculated to be 7.57, 6.95, and 6.63 for O_2BaF, O_2SrF, and O_2CaF, respectively. This variation indicates that O_2BaF possesses a higher dielectric polarizability, which reflects a stronger interaction between the electromagnetic field and the electronic structure compared with the other two compounds.

According to the Penn model, materials with larger static dielectric constants are generally expected to exhibit narrower electronic band gaps, while smaller $\varepsilon_1(0)$ values correspond to wider band gaps. The present results follow this inverse relationship, demonstrating that the calculated dielectric responses are fully consistent with the corresponding electronic energy gaps obtained from band-structure calculations.

An optical energy gap is clearly observed in the imaginary part of the dielectric function, $\varepsilon_2(\omega)$, for the majority-spin (spin-up) channel, confirming its semiconducting behavior. In contrast, the minority-spin (spin-down) channel exhibits a pronounced onset at low photon energies, which is characteristic of metallic behavior arising from allowed interband transitions across the Fermi level.

These optical features are in excellent agreement with the previously discussed band-structure and density-of-states (DOS) results, thereby unambiguously confirming the half-metallic nature of the O_2XF (X = Ca, Sr, Ba) compounds.

3.5.2. The optical parameters n (ω) and k (ω)are often discussed together

The index of refraction, denoted as n (ω), represents a crucial optical characteristic for investigating the prospective uses of a substance in the realm of optical and photonic apparatus [58]. This refractive index is mathematically expressed as:

$$n(\omega) = \frac{1}{\sqrt{2}}\left[\{\varepsilon_1^2(\omega) + \varepsilon_2^2(\omega)\}^{1/2} + \varepsilon_1(\omega)^{1/2}\right] \quad (11)$$

$$k(\omega) = \frac{1}{\sqrt{2}}\left[\{\varepsilon_1^2(\omega) + \varepsilon_2^2(\omega)\}^{1/2} - \varepsilon_1(\omega)^{1/2}\right] \quad (12)$$

The calculated refractive indices for O_2BaF, O_2SrF, and O_2CaF are presented in Figures 9–11(c), exhibiting behaviors analogous to the real component of the dielectric function, $\varepsilon_1(\omega)$. The refractive indices observed at zero frequency (static values) are recorded as n(0)=1.32 for O_2BaF, n(0)=1.31 for O_2SrF, and n(0)=1.32 for O_2CaF. As photon energy escalates, these indices reach maximum values: 1.85 for O_2BaF at an energy of 9.56 eV, 1.82 for O_2SrF at 9.83 eV, and 1.82 for O_2CaF at 8.66 eV. Refractive indices exceeding unity signal a reduction in the speed of photon propagation, directly resulting from their engagement with the electronic structure within the substance.

The refractive index is instrumental in understanding light bending, a property vital for applications in photoelectric and photonic hardware. An elevation in n(ω) signifies a greater temporal lag for photons, stemming from a more intense interplay with the material's electron density.

As illustrated in Figures 9–11(d), the extinction coefficient, denoted as κ(ω), mirrors the pattern of the imaginary component of the dielectric function, $\varepsilon_2(\omega)$, thereby quantifying the material's propensity for optical absorption. Greater magnitudes of κ(ω) correlate with increased absorption and subsequent fluorescence. For the O_2XF series, the maximal κ(ω) values are found near 18.08 eV (O_2BaF), 24.38 eV (O_2SrF), and 27.74 eV (O_2CaF), with noticeable abrupt increases in absorption (absorption edges) occurring around 13.24 eV, 11.50 eV, and 9.80 eV, respectively. O_2BaF displays the most pronounced peak, suggesting a stronger capacity for absorbing ultraviolet radiation and possibly yielding greater fluorescence in that specific spectral window. Conversely, across the low-energy spectrum encompassing the infrared and visible light ranges, κ(ω) approaches zero for all three compounds, indicating they are transparent in these spectral bands.

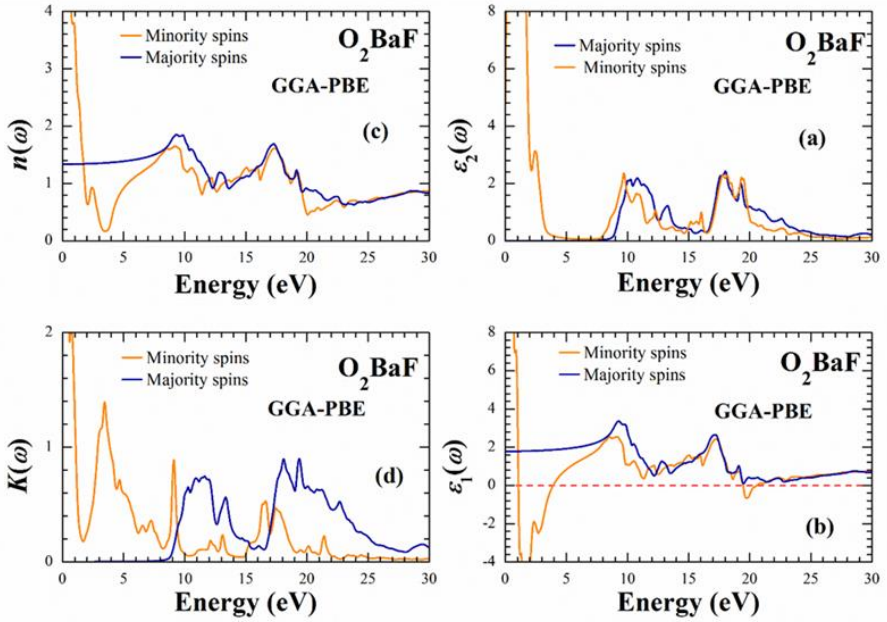

Fig. 9. Calculated spin up and down of (a) Imaginary part of dielectric function $\varepsilon_2(\omega)$, (b) Real part of dielectric function $\varepsilon_1(\omega)$, (c)refractive index $n(\omega)$, and (d) extinction coefficient $\kappa(\omega)$ as a function of photon energy for O_2BaF with GGA-PBE.

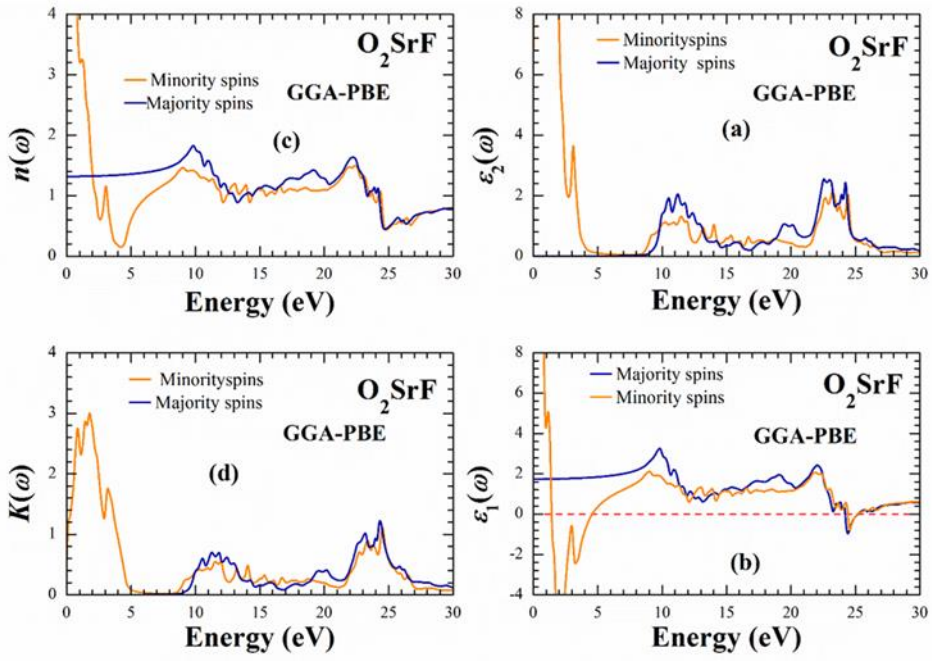

Fig.10. Calculated spin up and down of (a) Imaginary part of dielectric function $\varepsilon_2(\omega)$, (b) Real part of dielectric function $\varepsilon_1(\omega)$, (c)refractive index $n(\omega)$ and (d) extinction coefficient $\kappa(\omega)$ as a function of photon energy for O_2SrF with GGA-PBE.

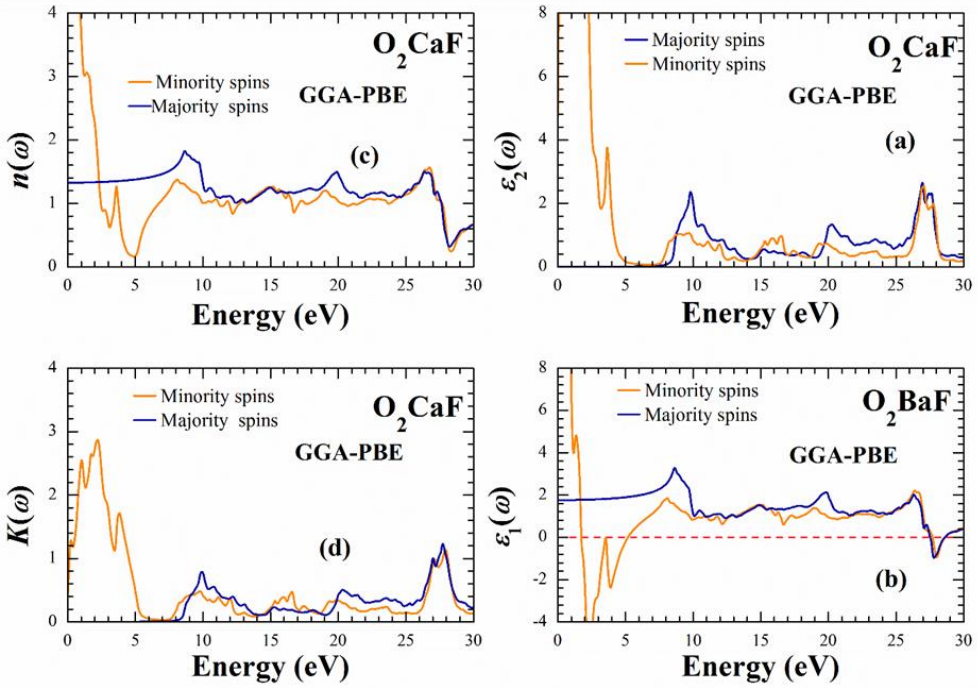

Fig.11. Calculated spin up and down of (a) Imaginary part of dielectric function $\varepsilon_2(\omega)$, (b) Real part of dielectric function $\varepsilon_1(\omega)$, (c)refractive index $n(\omega)$, and (d) extinction coefficient $\kappa(\omega)$ as a function of photon energy for O_2CaF with GGA-PBE.

4. Conclusions

This study has enhanced our understanding of the structural, mechanical, electronic, magnetic, and optical properties of the full-Heusler O_2XF (X = Ca, Sr, Ba) compounds. Using the full-potential linearized augmented plane wave (FPLAPW) method implemented in the WIEN2k code, we determined the most stable structure and evaluated the key structural parameters, including the lattice constant, bulk modulus, and its pressure derivative. The calculated elastic constants satisfy the cubic stability criteria of the Hg_2CuTi-type structure, confirming the mechanical stability and ductile nature of these compounds.

Electronic properties were examined through density of states (DOS) and band structure analyses using both the GGA-PBE and mBJ-GGA-PBE approaches. In all cases, the majority-spin (spin-up) channel exhibits an energy gap near the Fermi level, while the minority-spin (spin-down) channel remains metallic, indicating a robust half-metallic character with 100% spin polarization. The total magnetic moment of 3 μB per formula unit aligns well with the Slater–Pauling rule $M_{tot} = (24 - Z_{tot})\mu_B$.

The optical properties were examined over the photon-energy range of 0–30 eV. The dominant peak in the imaginary part of the dielectric function for the majority-spin channel originates from interband electronic transitions between the valence and conduction bands. These results, combined with the half-metallic electronic structure and mechanical robustness, indicate that the O_2XF compounds are promising candidates for spintronic and high-performance electronic applications, further supported by their favorable optical response.

As no prior theoretical or experimental reports are available for these materials, the present study constitutes the first comprehensive theoretical prediction of the structural, elastic, electronic, magnetic, and optical properties of the O_2XF series. Accordingly, this work provides a solid foundation for future experimental validation and may stimulate further research toward technological development and practical applications based on these full-Heusler compounds.

Funding Statement

This research received no specific grant from any funding agency.

Conflicts of interest

The authors declare that they have no known competing financial interests or personal relationships that could have appeared to influence the work reported in this paper.

Authors contribution statement

Conceptualization and study design : S. Benatmane, Data collection and experimentation: S. Benatmane ,Data analysis and interpretation: S. Benatmane, Manuscript writing and editing: S. Benatmane Supervision and project administration: S. Benatmane.

References

[1] Zarkevich, N.A., Singh, P., Smirnov, A.V. and Johnson, D.D., 2022. Effect of substitutional doping and disorder on the phase stability, magnetism, and half-metallicity of Heusler alloys. *Acta Materialia*, *225*, p.117477.

[2] Hirohata, A. and Lloyd, D.C., 2022. Heusler alloys for metal spintronics. *MRS Bulletin*, *47*(6), pp.593-599.

[3] Tavares, S., Yang, K. and Meyers, M.A., 2023. Heusler alloys: Past, properties, new alloys, and prospects. *Progress in Materials Science*, *132*, p.101017.

[4] Saleem, M. and Shakil, M., 2023. Determination of tunnelling magneto resistance of magnetic tunnel junction designed using Co_2TiAl Heusler alloy with MgO spacer layer. *Physica B: Condensed Matter*, *649*, p.414458.

[5] Shakil, M., Kousar, M., Gillani, S.S.A., Rizwan, M., Arshad, H., Rafique, M. and Zafar, M., 2022. First principle computation of half metallicity and mechanical properties of a new series of half Heusler alloys KMnZ (Z= B, Si, Ge, As) for spintronics. *Indian Journal of Physics*, *96*(1), pp.115-126.

[6] Idrissi, S., Khalladi, R., Ziti, S., El Mekkaoui, N., Mtougui, S., Labrim, H. and El Housni, I., 2019. The electronic and magnetic proprieties of the rare earth-based quaternary Heusler compound LuCoVGe. *Physica B: Condensed Matter*, *562*, pp.116-123.

[7] Chatterjee, S., Chatterjee, S., Giri, S. and Majumdar, S., 2021. Transport properties of Heusler compounds and alloys. *Journal of Physics: Condensed Matter*, *34*(1), p.013001.

[8] Abada, A., Amara, K., Hiadsi, S. and Amrani, B., 2015. First principles study of a new half-metallic ferrimagnets Mn2-based full Heusler compounds: Mn_2ZrSi and Mn2ZrGe. *Journal of Magnetism and Magnetic Materials*, *388*, pp.59-67.

[9] Zhang, Y.J., Liu, Z.H., Li, G.T., Ma, X.Q. and Liu, G.D., 2014. Magnetism, band gap and stability of half-metallic property for the quaternary Heusler alloys CoFeTiZ (Z= Si, Ge, Sn). *Journal of alloys and compounds*, *616*, pp.449-453.

[10] Behbahani, M.A., Moradi, M., Rostami, M. and Davatolhagh, S., 2016. First principle study of structural, electronic and magnetic properties of half-Heusler IrCrZ (Z= Ge, As, sn and sb) compounds. *Journal of Physics and Chemistry of Solids*, *92*, pp.85-93.

[11] Jaiganesh, G. and Jaya, S.M., 2015. Magnetism, electronic structure and half-metallic property of transition metal (V, Cr, Mn, Fe, Co) substituted Zn_3P_2 dilute magnetic semiconductors: An ab-initio study. *Computational Materials Science*, *102*, pp.85-94.

[12] Kervan, S. and Kervan, N., 2015. First-principles study on half-metallic ferromagnetism in the diluted magnetic semiconductor (DMS) $Al_{1-x}Mn_xP$ compounds. *Journal of Magnetism and Magnetic Materials*, *382*, pp.63-70.

[13] Rostami, M., Moradi, M., Javdani, Z. and Salehi, H., 2015. The electronic, magnetic and optical properties of Cr-doped MC (M= Si, Ge and Sn): a density functional theory approach. *Materials Science in Semiconductor Processing*, *38*, pp.218-227.

[14] Mahdy A.M.S., Lotfy K., El-Bary A., Sarhan H.H. (2021). Effect of rotation and magnetic field on a numerical-refined heat conduction in a semiconductor medium during photo-excitation processes, Eur. Phys. J. Plus. *136*, 1-17.

[15] Mahdy, A.M.S., Lotfy, K. and El-Bary, A., 2022. Thermo-optical-mechanical excited waves of functionally graded semiconductor material with hyperbolic two-temperature. *The European Physical Journal Plus*, *137*(1), p.105.

[16] Yasein, M.D., Mabrouk, N., Lotfy, K. and El-Bary, A.A., 2019. The influence of variable thermal conductivity of semiconductor elastic medium during photothermal excitation subjected to thermal ramp type. *Results in Physics*, *15*, p.102766.

[17] Ezzat, M.A. and El-Bary, A.A., 2016. Effects of variable thermal conductivity and fractional order of heat transfer on a perfect conducting infinitely long hollow cylinder. *International Journal of Thermal Sciences*, *108*, pp.62-69.

[18] Ezzat, M.A., El-Bary, A.A. and Morsey, M.M., 2010. Space approach to the hydro-magnetic flow of a dusty fluid through a porous medium. *Computers & Mathematics with Applications*, *59*(8), pp.2868-2879.

[19] Ezzat, M., El-Bary, A.A. and Ezzat, S., 2011. Combined heat and mass transfer for unsteady MHD flow of perfect conducting micropolar fluid with thermal relaxation. *Energy conversion and management*, *52*(2), pp.934-945.

[20] Hariharan, M. and Eithiraj, R.D., 2024. Structural, electronic, magnetic, and thermoelectric properties of newly predicted Fe2CoS and Ni2CoS alloys for spintronics applications: A DFT study. *Journal of Magnetism and Magnetic Materials*, *589*, p.171553.

[21] De Groot, R.A., Mueller, F.M., van Engen, P.V. and Buschow, K.H.J., 1983. New class of materials: half-metallic ferromagnets. *Physical review letters*, *50*(25), p.2024.

[22] Felser, C., Heitkamp, B., Kronast, F., Schmitz, D., Cramm, S., Dürr, H.A., Elmers, H.J., Fecher, G.H., Wurmehl, S., Block, T. and Valdaitsev, D., 2003. Investigation of a novel material for magnetoelectronics: Co2Cr0. 6Fe0. 4Al. *Journal of Physics: Condensed Matter*, *15*(41), p.7019.

[23] Kieven, D., Klenk, R., Naghavi, S., Felser, C. and Gruhn, T., 2010. I-II-V half-Heusler compounds for optoelectronics: Ab initio calculations. *Physical Review B—Condensed Matter and Materials Physics*, *81*(7), p.075208.

[24] Kautzsch, L., Mende, F., Fecher, G.H., Winterlik, J. and Felser, C., 2019. Are AuPd TM (T= Sc, Y and M= Al, Ga, In), Heusler Compounds Superconductors without Inversion Symmetry?. *Materials*, *12*(16), p.2580.

[25] Zeng, Q., Du, Z., Han, X., Wang, B., Wu, G. and Liu, E., 2024. Observation of atomically displacive transformation out of the boundary-reconstructive phase competition. *Acta Materialia*, *262*, p.119429.

[26] Dieny, B., Speriosu, V.S., Parkin, S.S., Gurney, B.A., Wilhoit, D.R. and Mauri, D., 1991. Giant magnetoresistive in soft ferromagnetic multilayers. *Physical Review B*, *43*(1), p.1297.

[27] Song, T., Cai, X., Tu, M.W.Y., Zhang, X., Huang, B., Wilson, N.P., Seyler, K.L., Zhu, L., Taniguchi, T., Watanabe, K. and McGuire, M.A., 2018. Giant tunneling magnetoresistance in spin-filter van der Waals heterostructures. *Science*, *360*(6394), pp.1214-1218.

[28] Cho, Y.M., Choo, W.K., Kim, H., Kim, D. and Ihm, Y., 2002. Effects of rapid thermal annealing on the ferromagnetic properties of sputtered Zn 1− x (Co 0.5 Fe 0.5) x O thin films. *Applied Physics Letters*, *80*(18), pp.3358-3360.

[29] Gilleßen, M. and Dronskowski, R., 2009. A combinatorial study of full Heusler alloys by first-principles computational methods. *Journal of computational chemistry*, *30*(8), pp.1290-1299.

[30] Nazemi, N., Ahmadian, F. and Boochani, A., 2023. Investigation of half-metallic properties of full-Heusler alloys of O2BaX (X= Na, K, Rb, and Cs). *Chemical Physics Letters*, *830*, p.140751.

[31] Ahmad, M., Murtaza, G., Khenata, R., Omran, S.B. and Bouhemadou, A., 2015. Structural, elastic, electronic, magnetic and optical properties of RbSrX (C, SI, Ge) half-Heusler compounds. *Journal of Magnetism and Magnetic Materials*, *377*, pp.204-210.

[32] Safavi, M., Moradi, M. and Rostami, M., 2017. Structural, electronic and magnetic properties of NaKZ (Z= N, P, As, and Sb) half-Heusler compounds: a first-principles study. *Journal of Superconductivity and Novel Magnetism*, *30*(4), pp.989-997.

[33] Zhao, J.S., Gao, Q., Li, L., Xie, H.H., Hu, X.R., Xu, C.L. and Deng, J.B., 2017. First-principles study of the structure, electronic, magnetic and elastic properties of half-Heusler compounds LiXGe (X= Ca, Sr and Ba). *Intermetallics*, *89*, pp.65-73.

[34] Rostami, M., 2018. Half-metallic property of the bulk and (001) surfaces of MNaCs (M= P, As) half-Heusler alloys: a density functional theory approach. *Surface Science*, *674*, pp.103-114.

[35] Benatmane, S. and Bouhafs, B., 2019. Investigation of new d0 half-metallic full-heusler alloys N2BaX (X= Rb, Cs, Ca and Sr) using first-principle calculations. *Computational Condensed Matter*, *19*, p.e00371.

[36] Benatmane, S., (2022). Theoretical investigations of structural, mechanical, electronic, and thermodynamic properties of BaNYO (Y= Mg, Ca, and Sr) alloys. *emergent mater*. *5* (6), pp. 1797-1817.

[37] Benatmane, S. and Cherid, S., 2020. First-Principles Study of Magnetism and Half-Metallic Properties of the d^0 Quaternary Heusler Alloys BaNYO (Y= K, Rb and Cs). *Journal of Experimental and Theoretical Physics Letters (JETP Letters)*.

[38] Blaha, P., Schwarz, K., Madsen, G. K. H., Kvasnicka, D. and Luitz, J., 2012. WIEN2k, An Augmented Plane Wave Plus Local Orbitals Program for Calculating Crystal Properties (Vienna University of Technology, Austria.

[39] Kulkova, S.E., Eremeev, S.V., Kakeshita, T., Kulkov, S.S. and Rudenski, G.E., 2006. The electronic structure and magnetic properties of full-and half-Heusler alloys. *Materials transactions*, *47*(3), pp.599-606.

[40] Perdew, J.P., Burke, K. and Ernzerhof, M., 1996. Generalized gradient approximation made simple. *Physical review letters*, *77*(18), p.3865.

[41] Koller, D., Tran, F. and Blaha, P., 2012. Improving the modified Becke-Johnson exchange potential. *Physical Review B—Condensed Matter and Materials Physics*, *85*(15), p.155109.

[42] Murnaghan, F.D., 1944. The compressibility of media under extreme pressures. *Proceedings of the National Academy of Sciences*, *30*(9), pp.244-247.

[43] Benatmane, S., Affane, M., Bouali, Y., Bouadjemi, B., Cherid, S. and Benstaali, W., 2023. Phase stability, mechanical, electronic, magnetic and thermodynamic properties of the Pd2PrX (X= Cl, F) compounds: An Ab-initio study. *Revista mexicana de física*, *69*(1), pp.0-0.

[44] Benatmane, S., 2021. Theoretical investigations of structural, mechanical, electronic, and thermodynamic properties of BaNYO (Y = Mg, Ca, and Sr) alloys, *Emergent Materials,* 5, pp, 1797-1817.

[45] Benatmane S., Beldi, L., Bendaoud, H., Méçabih, S., Abbar, B. and Bouhafs, B., 2019. Spin-polarized optical properties of half-metallic binary XBi (X = Ca, Sr and Ba) compounds in zinc blende and wurtzite phases, *Indian Journal Physics,* 93, pp, 627-638

[46] Benatmane, S., 2025. Computational Determination of Structural, Electronic, Magnetic, Elastic, and Optical Properties of $BaCaN_3$ and $BaSrN_3$ Perovskites as Potential Spintronic Materials." *Strength of Materials,* 57 (3), pp, 646-657.

[47] Ouardi, S., Fecher, G.H., Balke, B., Beleanu, A., Kozina, X., Stryganyuk, G., Felser, C., Klöß, W., Schrader, H., Bernardi, F. and Morais, J., 2011. Electronic and crystallographic structure, hard x-ray photoemission, and mechanical and transport properties of the half-metallic Heusler compound Co 2 MnGe. *Physical Review B—Condensed Matter and Materials Physics*, *84*(15), p.155122.

[48] Zhang, Y.Z., Wang, Y., Cheng, T., Lai, W.Y., Pang, H. and Huang, W., 2015. Flexible supercapacitors based on paper substrates: a new paradigm for low-cost energy storage. *Chemical Society Reviews*, *44*(15), pp.5181-5199.

[49] Anderson, O.L., 1963. A simplified method for calculating the Debye temperature from elastic constants. *Journal of Physics and Chemistry of Solids*, *24*(7), pp.909-917.

[50] Johnston, I., Keeler, G., Rollins, R. and Spicklemire S., 1996. Solids state physics simulations, the consortium for upperlevel physics software. *Wiley, New York*.

[51] Newnham, R.E., 2005. *Properties of materials: anisotropy, symmetry, structure*. Oxford university press.

[52] Feng, J., Chen, J.C., Xiao, B., Zhou, C.T., Hong, Z.J. and Zhou, R., 2009. Stability, thermodynamic and mechanical properties of the compounds in the Ag–Sn–O system. *Physica B: Condensed Matter*, *404*(16), pp.2461-2467.

[53] Schreiber E., Anderson, O.L., Soga, N. and Bell, J.F., 1975. Elastic constants and their measurement, *Journal of Applied Mechanics*, 42, pp.747-748.

[54] Daoud, S., Loucif, K., Bioud, N., Lebgaa, N. and Belagraa, L., 2012. Effect of hydrostatic pressure on the structural, elastic and electronic properties of (B3) boron phosphide. *Pramana*, *79*(1), pp.95-106.

[55] Lin, H., Wray, L.A., Xia, Y., Xu, S., Jia, S., Cava, R.J., Bansil, A. and Hasan, M.Z., 2010. Half-Heusler ternary compounds as new multifunctional experimental platforms for topological quantum phenomena. *Nature materials*, *9*(7), pp.546-549.

[56] Skaftouros, S., Özdoğan, K., Şaşıoğlu, E. and Galanakis, I., 2013. Generalized Slater-Pauling rule for the inverse Heusler compounds. *Physical Review B—Condensed Matter and Materials Physics*, *87*(2), p.024420.

[57] Abada, A., Amara, K., Hiadsi, S. and Amrani, B., 2015. First principles study of a new half-metallic ferrimagnets Mn2-based full Heusler compounds: Mn2ZrSi and Mn2ZrGe. *Journal of Magnetism and Magnetic Materials*, *388*, pp.59-67.

[58] Benatmane, S.A.A.D.I.Y.A. and Hezil-Ziane, S.A.M.I.R.A., 2024. DFT study of BaKN3 and BaRbN3 Perovskites: Revealing their Mechanical, Optoelectronic, and Magnetic Properties. *Revista Cubana de Física*, *41*(2), pp.103-112.

[59] Benosmane, W., Benatmane, S., Bentata, R. and Benstaali, W., 2021, June. Calculation of Structural, Electronic and Optical Properties of Double Perovskite Ca2CrNbO6. In *Spin* (Vol. 11, No. 02, p. 2150012). World Scientific Publishing Company.